JACS
JOURNAL OF THE AMERICAN CHEMICAL SOCIETY
pubs.acs.org/JACS
Article

Chemi-Impeditive Sensing Platform Based on Single-Walled Carbon Nanotubes

Seok Hee Han, Thomas N. Pioch, and Timothy M. Swager*

Cite This: J. Am. Chem. Soc. 2024, 146, 31486−31496
Read Online
ACCESS | Metrics & More | Article Recommendations | Supporting Information

ABSTRACT: Chemical sensing methodology based on electrochemical impedance spectroscopy (EIS) targeting analytes in aqueous samples on functionalized single-walled carbon nanotube (SWCNT) is reported. The SWCNT in contact with electrolyte shows unique impedance spectra that cannot be analyzed with classical equivalent circuit models. Inspired by the charge transport property of mixed ionic-electronic conductors, we propose an equivalent circuit based on transmission line model (TLM), by which the impedance of the CNT-electrolyte system can be analyzed to track down all the equivalent circuit parameters. By combining multiple pieces of information, which are technically immeasurable with conventional chemiresistive or chemicapacitive techniques, several analyte species responding to the sensor can be differentiated from each other. We demonstrate the "chemi-impeditive" concept on chemically modified SWCNTs for detecting perfluoroalkyl substances (PFAS) in aqueous solutions. The EIS coupled with a fluorination chemistry on SWCNT surface provides unique changes in equivalent circuit components for each PFAS, i.e., changes in CNT and solution resistances, as well as interfacial CNT-solution capacitance, through which perfluorooctanesulfonic acid, perfluorooctanoic acid, hexafluoropropylene oxide dimer acid, and perfluorobutanesulfonic acid are detected in a discriminative manner. The new impedimetric method opens up new vistas in chemical sensing in that the EIS analysis provides an additional dimension of information beyond the single resistance or capacitance typically measured by many conventional types of sensors.

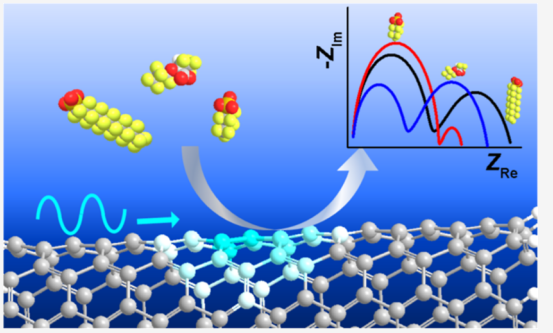

INTRODUCTION

Chemical sensors based on single-walled carbon nanotubes (SWCNTs) are a promising platform due to their low fabrication costs, low power requirement, low operating temperature, portability and ease of minimization.[1−3] Conventionally, the presence of target analytes induces a sensitive change in conductance (chemiresistive mode), or in capacitance (chemicapacitive mode) of the SWCNT network (Figure 1).[2] In chemiresistive mode, the conductance is generally modulated by electrical conduction between individual SWCNTs, or by changes in the charge carrier concentration and mobility of semiconducting SWCNTs as a result of charge transfer between analytes and SWCNTs or carrier pinning/unpinning. The chemicapacitive method relies on changes in gate capacitance or quantum capacitance of SWCNTs, which are caused by charge transfer from adsorbate species or adsorbate polarization under a fringing electric field.[4−6] A variety of sensing platforms are possible depending on the selectors and sensing mechanisms and include chemiresistive sensors for hydrogen sulfide,[7] methane,[8,9] BTX vapors,[10] chemical warfare agents,[11−13] and anions,[14,15] and chemicapacitive sensors for warfare agents[16,17] and other gas molecules.[4−6,18] Despite promising sensing performance and wide applicability, there are technological limitations. Most of these sensors have been designed to target analytes in the vapor phase, preferably without humidity, owing to the sensitivity of charge mobility to water and the lack of understanding of the CNT-liquid interface. Notably, such sensors offer only a single type of information about the system: apparent resistance (R_{app}) or capacitance (C_{app}), typically measured by applying DC or AC voltage to the device. As a result, these approaches overlook the existence of multiple resistive and capacitive components within the CNT network (Figure 1). If the system consists of multiple components that undergo changes during the sensing process, they cannot be distinguished from one another solely through DC or single-frequency AC measurements.

Electrochemical impedance spectroscopy (EIS) offers a full description of the actual equivalent circuit of the system.[19] Impedance values obtained at various frequencies are generally displayed as complex curves, which can be rich in information when analyzed using proper physicochemical models.

Received: June 12, 2024
Revised: October 23, 2024
Accepted: October 29, 2024
Published: November 6, 2024

https://doi.org/10.1021/jacs.4c07986
J. Am. Chem. Soc. 2024, 146, 31486−31496

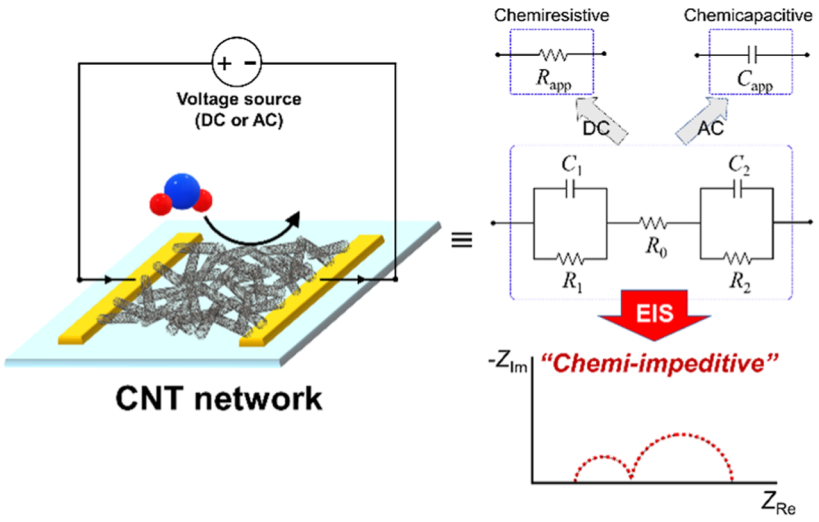

Figure 1. Schematic description comparing chemi-impeditive sensing using CNTs with conventional chemiresistive and chemicapacitive methods. Equivalent circuit of the CNT network was chosen arbitrarily for demonstration purposes. R_{app} and C_{app} represent apparent resistance and capacitance of the entire system, respectively.

Although there are several reports on CNT-based chemical sensors employing EIS,[20−22] it predominantly functioned as a supplementary analytical technique in most cases, either corroborating the main sensor signals obtained from DC measurements or examining additional factors that influence the sensing process. In this work, we detail a "chemi-impeditive" sensing methodology based on a functionalized SWCNT network submerged in an aqueous solution containing analytes. EIS is utilized to leverage comprehensive information on equivalent circuit components for the discriminative detection of multiple analytes, as illustrated in Figure 1. Drawing inspiration from the transport property of mixed ionic-electronic conductors (MIECs), we modeled the SWCNT-electrolyte system with a transmission line model (TLM) involving the resistances of sample solution and CNT layer, and the capacitive elements accounting for the system dielectric capacitance and the interfacial CNT-electrolyte capacitance. Combined with the analytical impedance expression of the TLM, EIS can track down changes in all the circuit component parameters over time during the sensing process.

To demonstrate the chemi-impeditive detection platform as proof-of-concept, we chose four different perfluoroalkyl substances (PFAS) as target analytes: perfluorooctanesulfonic acid (PFOS), perfluorooctanoic acid (PFOA), hexafluoropropylene oxide (HFPO) dimer acid (also referred to as GenX), and perfluorobutanesulfonic acid (PFBS). PFAS are a large group of artificial perfluorinated chemicals.[23] Since the 1940s, they have been widely used across numerous academic and industrial applications owing to their oil and water-resistant properties.[24−27] Because of the high chemical stability of perfluoroalkyl groups, however, they are called "forever chemicals" as they resist decomposition in the environment as well as in human bodies. The persistence of these chemicals poses a global problem with increasing evidence of adverse health effects and environmental influences.[28−30] Accordingly, it is of paramount importance to sensitively detect multiple types of PFAS from water samples, preferably without expensive instrumentations and complicated procedures for sample preparation.[31−33] To this end, we apply our chemi-impeditive method to the SWCNT surface covalently functionalized with perfluoroalkyl groups and amine moieties via cycloaddition reactions of azomethine ylides.[34] The hydrophobic and electrostatic interactions between PFAS and the fluorinated SWCNT surface enable trace detection of the two major PFAS at concentrations of ca. 4 ppb for PFOS and ca. 36 ppb for PFOA. Different device fabrication strategies have been studied,[2] and most often devices are prepared by the deposition of dispersions of nanotubes. Unbundled SWCNTs provide the best sensor performance, and we have made use of a random intertube arrangement produced from drop casting dispersions to prevent bundling. The quantity of SWCNTs deposited between electrodes is determined by creating a favorable resistivity between electrodes for the measurements, which is generally between 1 and a 1000 kΩ. Commercial 6,5-inriched SWCNTs are in our experiments, and the metallic character of the minority tubes is quenched by covalent functionalization to produce compositions that can be assumed to contain only semiconductive tubes. We further demonstrate the capability of EIS to furnish comprehensive information concerning all equivalent circuit parameters included in the model during the sensing process of each PFAS, enabling the discriminative detection of PFOS, PFOA, as well as their replacements, PFBS and GenX.

RESULTS AND DISCUSSION

As depicted in Figure 2a, our SWCNT-based chemi-impeditive sensing device has a structure very similar to typical chemiresistive or chemicapacitive devices.[5,7,12,14,35−39] The active CNT layer is situated between two gold electrodes, while a reservoir cylinder to contain the sample solution is placed over the sensing material. Central to the impedance analysis is the proper modeling of the CNT-solution system with an equivalent circuit capable of accounting for the entire system. Figure 2b displays Nyquist plots of the pristine SWCNT (p-SWCNT) layer without an electrolyte solution, and with a 1 mM KCl(aq) in the reservoir. In the absence of solution, the impedance response manifests as a single semicircle, which is perfectly fit with a parallel *RC* circuit, where R_{CNT} indicates the resistance of CNT network, and C_{diel} the total dielectric capacitance including parasitic capacitance

https://doi.org/10.1021/jacs.4c07986
J. Am. Chem. Soc. 2024, 146, 31486−31496

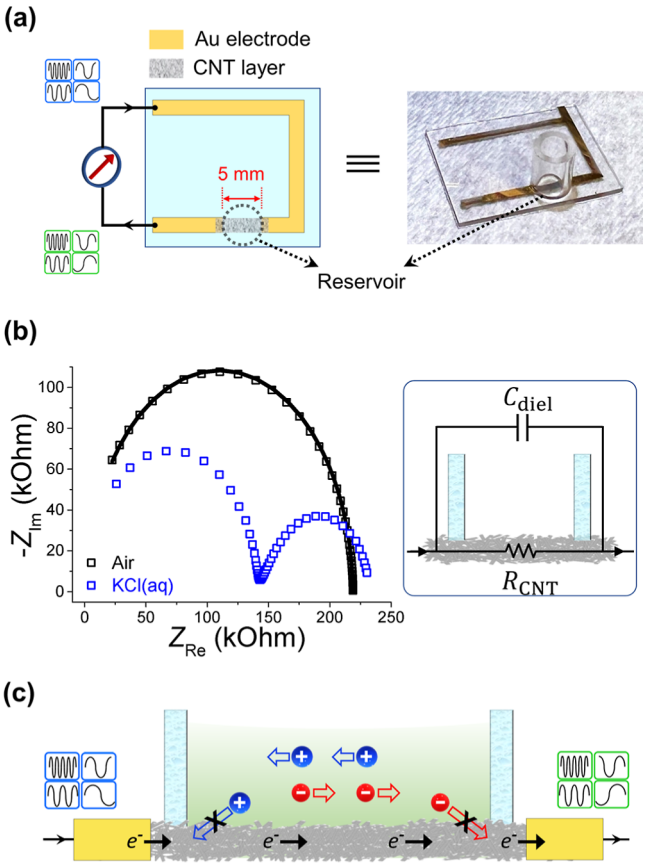

Figure 2. (a) Schematic of SWCNT-based chemi-impeditive sensing platform. A reservoir cylinder is placed on CNT film for injecting sample solution. (Inset: a photograph of a device fabricated) (b) Nyquist plots recorded on a p-SWCNT-based device with no solution (black), and with 1 mM KCl(aq) (blue) in reservoir. Black solid line represents a simulated impedance response from mathematical fitting. (Inset: parallel RC circuit employed for fitting) (c) graphical illustration of charge transport property of a CNT immersed in an electrolyte solution.

of the instrument, geometrical capacitance of the device, and capacitance of the CNT network (see also Figure S1). In the presence of an electrolyte solution, the Nyquist plot turns into what appears to be a combination of two *RC* semicircles, although the plot cannot be fit with any of the classical equivalent circuits based on *R* and *C*. To further investigate the CNT-solution system, we obtained Nyquist plots of a disconnected p-SWCNT film in the presence of aqueous KCl solution with varying concentrations in the reservoir, as described in Figure S2. The system can be modeled with two interfacial CNT-electrolyte impedances (Z_1 and Z_2) and an ionic resistance (R_{ion}), all connected in series. The Nyquist plots exhibit a high-frequency semicircle and low-frequency features resembling a constant phase element (CPE)[40] (Figure S2b). The high-frequency semicircle conforms to a parallel *RQ* circuit (Figure S2c), yielding circuit component parameters summarized in Table S1. The CPE impedance is expressed as below

$$\hat{z} = \frac{1}{(j\omega)^{\phi} Q} \tag{1}$$

where $0 \leq \phi \leq 1$ is the dimensionless CPE exponent and Q the capacitance parameter. The effective capacitance of CPE, C_{eff} of a parallel *RQ* circuit, was calculated using the equation below[40,41]

$$C_{eff} = \frac{(Q \times R)^{1/\phi}}{R} \sin\left(\frac{\phi\pi}{2}\right) \tag{2}$$

R changed sensitively with [KCl], whereas C_{eff} varied only slightly (ca. 1−2 pF), which is similar to C_{diel} from Figure S1. Thus, the low-frequency region corresponds to the impedance of the CNT-electrolyte interface, where $-Z_{Im}$ keeps increasing as the frequency decreases. This indicates that there is no faradaic charge transfer between CNT network and electrolyte, and this polarizable interface can thus be practically considered as capacitor or CPE.

The in-depth equivalent circuit analysis allows us to treat the CNT-electrolyte system as a conducting material with both ions and electrons as charge carriers, wherein only electrons pass through the sandwiching electrodes, as illustrated in Figure 2c. In terms of charge conduction properties, the CNT-electrolyte system behaves analogous to MIECs contacted with electrodes that are ideally ion blocking and reversibly transport electrons (see Figure S3).[42−44] The AC impedance response of such MIECs has been comprehensively studied by several researchers,[44−48] who employed a TLM containing its ionic and electronic resistances, dielectric capacitance, and the chemical capacitance, in order to model the MIEC whose thickness is much greater than the Debye length. Similarly, we applied the TLM to our CNT-electrolyte system with the resistances of the solution and CNT network, R_{ion} and R_{CNT}, the CPEs for nonideal dielectric capacitance and interfacial CNT-electrolyte capacitance, Q_{diel} and Q_{dl}, as illustrated in Figure 3a. The impedance response of this TLM, Z_{TLM}, can be written as[47,49]

$$Z_{TLM} = (R_{CNT} - R_{par}) \frac{\tanh\sqrt{\frac{(j\omega)^{\phi_{dl}}(R_{CNT}+R_{ion})Q_{dl}}{4}}}{\sqrt{\frac{(j\omega)^{\phi_{dl}}(R_{CNT}+R_{ion})Q_{dl}}{4}}} \tag{3}$$

where R_{par} is the parallel summation of R_{CNT} and R_{ion}, as presented in eq 4

$$\frac{1}{R_{par}} = \frac{1}{R_{CNT}} + \frac{1}{R_{ion}} \tag{4}$$

Figure 3b displays a typical impedance spectrum of this TLM, which comprises a high-frequency semicircle followed by the Warburg feature at lower frequencies with two characteristic points, R_{par} and R_{CNT}. As depicted in Figure 3c, we measured impedance spectra of a p-SWCNT film immersed in aqueous KCl solution of several different concentrations to confirm that our CNT-electrolyte system is properly modeled. They all aligned well with the aforementioned TLM, and the estimated equivalent circuit parameters are summarized in Table S2. As shown in Figure 3d, R_{ion} decreases sensitively as [KCl] increases, while R_{CNT} marginally increases, which is reasonable because the ionic resistance of solution is directly related to the salt concentration. The slight change in R_{CNT} is consistent with observations in previous literature,[50] which reported that SWCNT conductivity tends to decrease as [KCl] increases. C_{eff} of the TLM was calculated using the equation below[47]

https://doi.org/10.1021/jacs.4c07986
J. Am. Chem. Soc. 2024, 146, 31486−31496

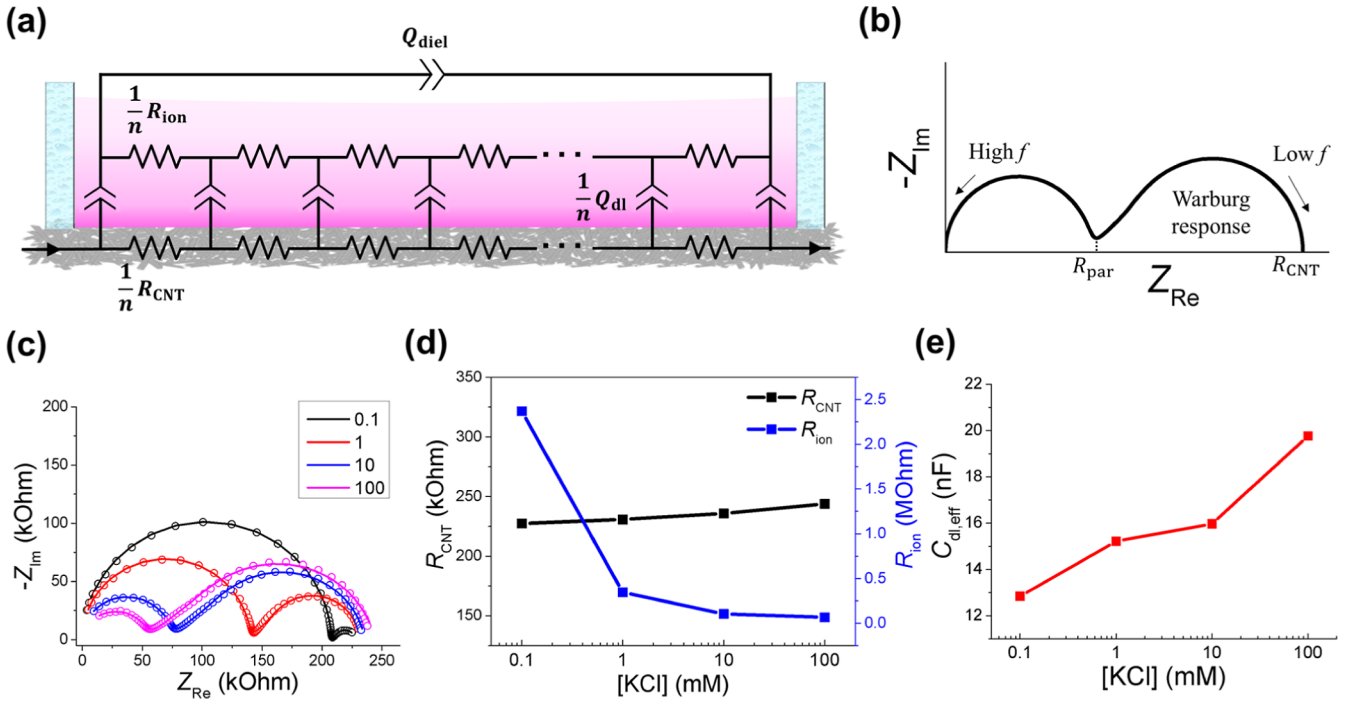

Figure 3. (a) Proposed equivalent circuit for the CNT-electrolyte system based on transmission line model (TLM). (b) A theoretical impedance response for the TLM in (a). (c) Complex plane plots for impedance responses measured on a p-SWCNT-based sensing device in the presence of KCl(aq) of varying concentrations. Solid lines indicate simulated curves calculated from complex nonlinear fitting; (d) R_{CNT}, R_{ion}, and (e) $C_{dl,eff}$ estimated from mathematical fitting for each [KCl] in (c).

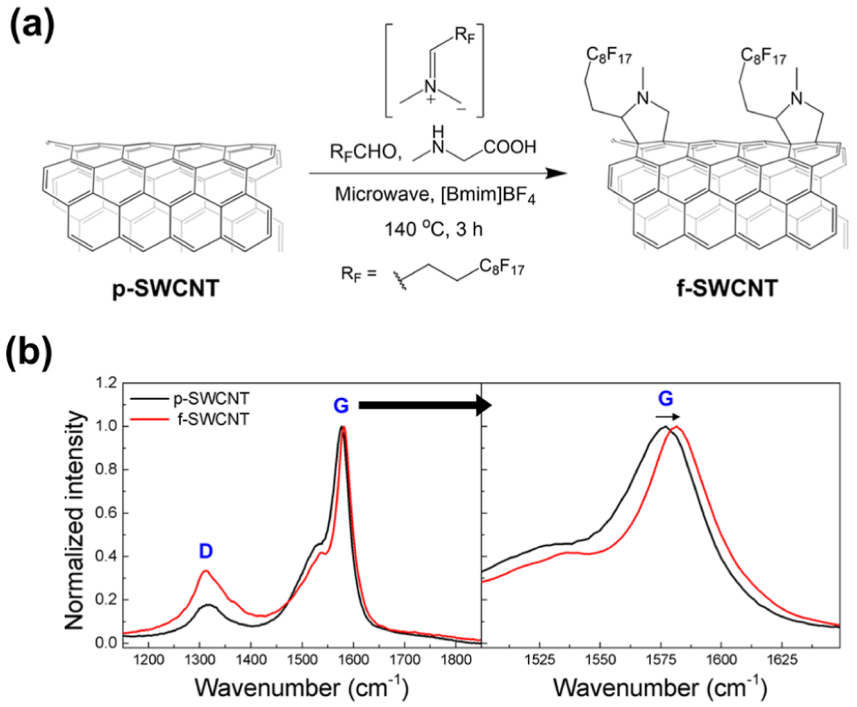

Figure 4. (a) Synthesis of f-SWCNT via azomethine ylide cycloaddition on p-SWCNT surface with perfluorinated aldehyde. (b) D- and G-bands from Raman spectra of p-SWCNT (black) and f-SWCNT (red) dropcasted on a glass slide (excitation at 532 nm).

$$C_{eff} = Q_{dl}^{1/\phi_{dl}} \left(\frac{R_{CNT} + R_{ion}}{4} \right)^{1/\phi_{dl}-1} \quad (5)$$

The gradual increase in C_{eff} in Figure 3e is also reasonable in that the differential double-layer capacitance from the Gouy–Chapman theory is predicted to increase as the electrolyte concentration increases.[51]

As the appropriate circuit model for impedance analysis of the CNT-electrolyte system was established, we developed an aqueous PFAS detection platform for demonstration by chemically modifying the SWCNT surface with perfluorooctyl

https://doi.org/10.1021/jacs.4c07986
J. Am. Chem. Soc. 2024, 146, 31486−31496

groups. As illustrated in Figure 4a, we conducted an azomethine ylide cycloaddition reaction as reported by Guryanov et al.[34] to introduce amine and perfluorooctyl groups onto the p-SWCNT for selective PFAS detection. Upon microwave irradiation, the azomethine ylide generated from perfluoroalkyl aldehyde and sarcosine underwent cycloaddition on the p-SWCNT surface in the presence of the ionic liquid, [bmim]BF_4, as solvent (bmim = 1-methyl-3-*n*-butyl imidazolium). The fluorinated SWCNT (f-SWCNT) obtained was dispersible only in hexafluoroisopropanol after sonication (see Figure S4), indicating successful fluorination of the CNT surface. Both the p-SWCNT and f-SWCNT dispersions could be easily dropcast and dried on slide glass to form random CNT networks (Figure S5). To corroborate the fluorination of SWCNT surface, the f-SWCNT was first characterized by Raman spectroscopy (532 nm excitation, Figure 4b). The D/G band intensity ratio increased from 0.175 to 0.332 after functionalization, indicating the introduction of defects. This conforms with the cycloaddition chemistry given that the reaction leads to the rehybridization of carbon atoms from sp^2 to sp^3 on the SWCNT surface, which lowers the electronic delocalization. Furthermore, an upshift of the G-band wavenumber was observed, which is also reasonable because the charge transfer arising from doping SWCNT with electron-withdrawing species induces an increase the bond strength in the graphene network.[52] The introduction of amine and perfluoroalkyl group was further probed by X-ray photoelectron spectroscopy (XPS) (Figure S6). As presented in Figure S6a, the survey spectrum contained sharp F 1s, N 1s, and C 1s peaks, which supports the functionalization of the SWCNT by perfluorooctyl groups bound to pyrrolidine moieties. A high-resolution N 1s scan in Figure S6b revealed four components with binding energies, the smallest of which had a binding energy of 403.7 eV and likely corresponds to a small amount (<0.3 atomic %) of N-oxides.[53] Another component with binding energy 401.9 eV matches well with the N 1s binding energies of imidazolium-based ionic liquids in the literature,[54] suggesting the presence of residual [bmim]BF_4 from the functionalization reaction. The component at 400.6 eV is similar to the N 1s binding energy of the amine nitrogen in the sarcosine starting material, as shown in Figure S6c. The last component at 398.9 eV is consistent with the binding energy of certain tertiary amines in the NIST XPS database,[55] and is therefore likely associated with the pyrrolidine nitrogen in the covalently attached functional group. This peak was used to calculate a degree of functionalization (DOF) of 4.23 functional groups (FGs) per 100 CNT carbon atoms.

Having obtained the f-SWCNT for PFAS detection, we first investigated the individual sensor responses to PFOS, PFOA, GenX, and PFBS in aqueous solution using chemiresistive (DC) measurement. The response is defined as $[(R - R_0)/R_0]$ (%), where R_0 and R are the DC resistance under the baseline solution (30 μL) and after PFAS solution spike (7.5 μL). Our sensor exhibited p-type responses (increase in hole carriers) to all four PFAS (Figure 5a). A proximate binding of PFAS anions to f-SWCNT, facilitated by the protonation of pyrrolidine moieties and fluorophilic interactions, likely results in reduced electron-donating charge transfer and electrostatic interactions due to the displacement of chloride ions by PFAS. This process leads to an increase in hole carriers, thereby enhancing the CNT conductivity. The sensor easily reached a stable signal baseline before sample injection, and demonstrated stable dosimetric responses to all PFAS species. We

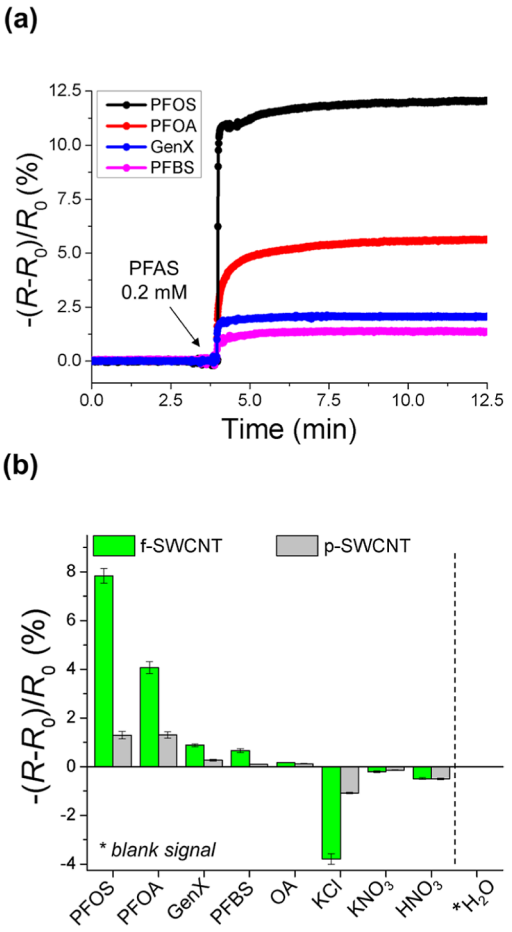

Figure 5. (a) Typical chemiresistive responses of f-SWCNT to four PFAS: PFOS (black), PFOA (red), GenX (blue), and PFBS (magenta). PFAS spike was 0.2 mM. (b) Summary of chemiresistive responses of f-SWCNT and p-SWCNT upon addition of various electrolyte species ($N = 4$). Analyte spike was 0.02 mM. Note that the addition of DI water into the reservoir showed negligible resistance changes in all cases.

employed 1 mM HCl(aq) as the baseline solution to maximize sensor response by further facilitating protonating amine groups on the CNT surface, enabling electrostatic and hydrophobic interactions between anionic PFAS and ammonium ions (see Figure S7). The sensor showed lower responses when other non-PFAS acids were used as the baseline solution (Figure S8). The sensor response likely depends on the type of baseline acid, as both the PFAS and the conjugate base of the baseline acid can interact with the cationic f-SWCNT surface. A negligible sensor signal was observed under 1 mM KCl(aq) as the baseline solution (Figure S9), which highlights the importance of protonating surface amine groups. As for the optimum HCl concentration, the highest response was observed near 1 mM (Figure S10), presumably because both the protonation of surface amines and the deprotonation of PFAS counterions are crucial for obtaining high PFAS affinity on the f-SWCNT surface. The sensor response decreased in the order of PFOS > PFOA > GenX > PFBS. Fluorophilicity of each PFAS species may be one of the primary factors determining sensor responses. According to computational studies on fluorophilicity,[56] the overall fluorine content of the molecule is the most important property, consistent with the observed sensitivity order (Figure S11). To investigate the

https://doi.org/10.1021/jacs.4c07986
J. Am. Chem. Soc. 2024, 146, 31486−31496

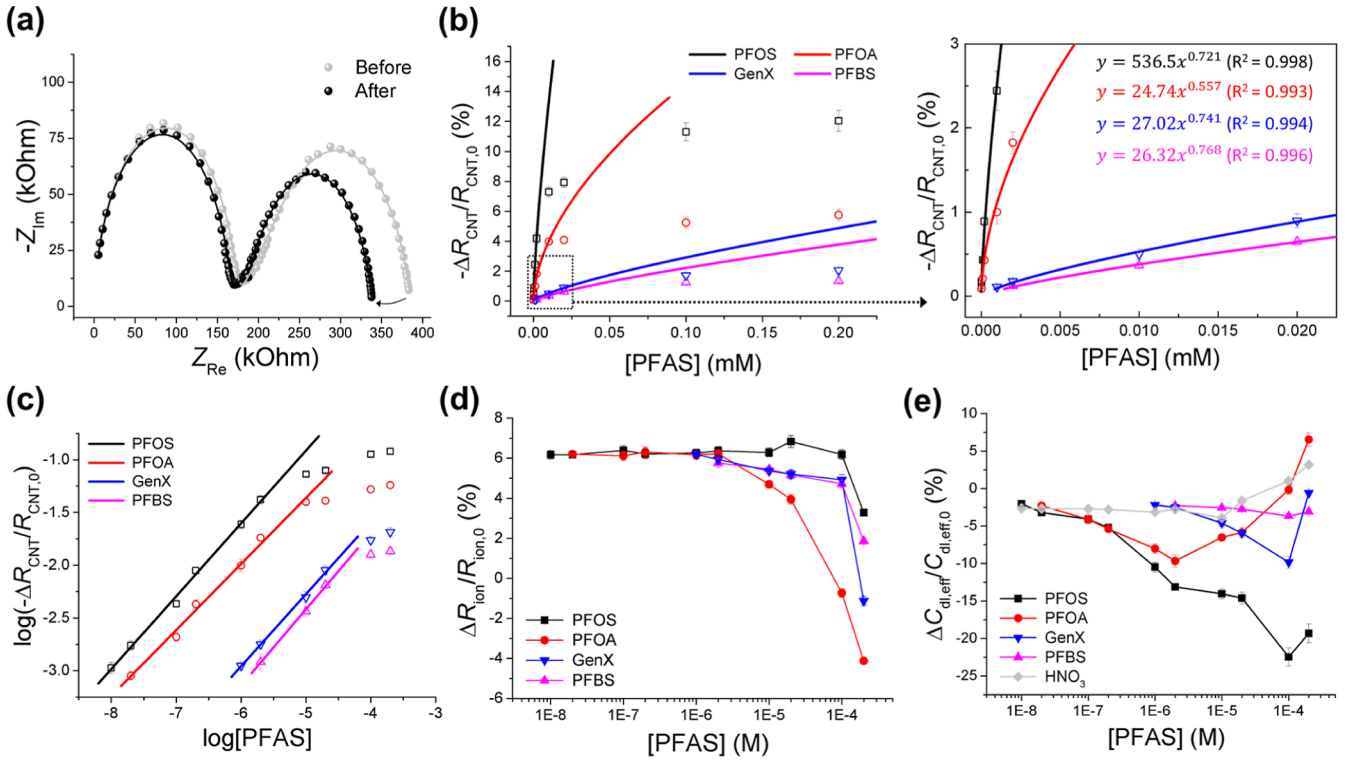

Figure 6. (a) Nyquist plots obtained before (gray) and after (black) 0.2 mM PFOS spike onto f-SWCNT. Solid line represents a fitted curve for each impedance response. Summary of chemi-impeditive responses of (b,c) R_{CNT}, (d) R_{ion}, and (e) $C_{dl,eff}$ on f-SWCNT to different concentrations of PFOS (black), PFOA (red), GenX (blue), and PFBS (magenta) ($N = 4$). (c) log–log plot of the response curve in (b). Solid lines in (b,c) are curves fitted with Freundlich model. Note that several data points at high concentration range were excluded from fitting. Chemi-impeditive responses of $C_{dl,eff}$ to different concentrations of HNO_3 (gray) were included in (e) for comparison.

Table 1. Summary of Equivalent Circuit Parameters Calculated from Nyquist Plots in Figure 6a[a]

	Q_{diel}	ϕ_{diel}	$C_{diel,eff}$ (F)	R_{CNT} (Ω)	R_{ion} (Ω)	Q_{dl}	ϕ_{dl}	$C_{dl,eff}$ (F)
before	2.94×10^{-11}	0.947	1.47×10^{-11}	3.86×10^{5}	3.08×10^{5}	1.66×10^{-6}	0.838	1.31×10^{-6}
after	2.75×10^{-11}	0.952	1.46×10^{-11}	3.38×10^{5}	3.19×10^{5}	1.33×10^{-6}	0.865	1.05×10^{-6}

[a]TLM-based equivalent circuit in Figure 3a was used for fitting.

effect of functional group coverage on sensing response, we formulated three additional fluorinated SWCNTs with varying DOFs, designated as f_1-SWCNT, f_2-SWCNT, and f_3-SWCNT (Table S3). The XPS analysis revealed high-resolution N 1s spectra with four components, similar to those observed for f-SWCNT (Figure S12). The area of the pyrrolidine component near 399.0 eV was used to calculate DOF values of 2.35, 1.87, and 1.39 FGs per 100 CNT carbon atoms for f_1-, f_2-, and f_3-SWCNT, respectively. The differences in the amount of aldehyde starting material caused variation in DOFs, while the lower reaction temperature yielded significantly lower DOFs for all three samples than the 4.23 FGs per 100 CNT carbon atoms observed in f-SWCNT. The sensor devices made from f_1-, f_2-, and f_3-SWCNT were observed to be less sensitive than the f-SWCNT-based device, with response curves shifting toward higher PFAS concentrations (Figure S13). The sensor response followed the order of f-SWCNT > f_1-SWCNT > f_2-SWCNT > f_3-SWCNT, which correlates with the order of DOF. This finding supports that electrostatic and fluorophilic interactions between PFAS and the CNT surface are the primary factors determining sensor response. A 1 mM solution of strong acid (pH = 3), i.e., HCl(aq), is sufficiently acidic to protonate surface pyrrolidine groups and the PFAS species with low pK_a values, PFOS ($pK_a = -3.27$), PFOA ($pK_a = -0.2$), and PFBS ($pK_a = 0.14$),[57] are present as anions in the solution. GenX, with a pK_a of 2.84,[58] is relatively close to the solution pH of 3, which may have influenced the sensor response order above. Figure 5b implies that the CNT functionalization employed was effective for detecting PFAS molecules compared to the p-SWCNT. The f-SWCNT exhibited much higher affinity for PFAS species, particularly PFOS and PFOA, than for the other ionic species and octanoic acid (OA), the nonfluorinated equivalent of PFOA. Adding nonfluorous electrolytes such as KCl and KNO_3 resulted in an increase in R_0, with the R_0 response of f-SWCNT being greater than or similar to that of p-SWCNT. Considering the smaller response to KNO_3 compared to HNO_3, the distinct increase in resistance for KCl may primarily be attributed to Cl^- ions. This anion dependence could be related to the cationic nature of f-SWCNT surface, which has protonated amine groups and physisorbed oxygen that creates hole carriers and causes SWCNTs to have p-type character. The conductivity of f-SWCNT did not change upon addition of the blank solution, deionized (DI) water with no additional ionic species dissolved. Although the p-SWCNT is slightly responsive to the PFAS species, the response is very sluggish and difficult to analyze accurately due to severe baseline drift (Figure S14), rendering it unsuitable for subsequent EIS analysis. Classical

https://doi.org/10.1021/jacs.4c07986
J. Am. Chem. Soc. 2024, 146, 31486–31496

EIS cannot obtain valid EIS spectra for such systems with high nonstationarity.

The sensing performance of our f-SWCNT-based device was examined by employing EIS before and after injection of PFAS solutions into the baseline solution. Figure 6a presents a typical impedance response upon a PFOS spike of 200 μM into the reservoir. The impedance plots were well fit to the TLM-based equivalent circuit in Figure 3a, which provides estimated circuit parameter values: Q_{diel}, ϕ_{diel}, R_{CNT}, R_{ion}, Q_{dl}, and ϕ_{dl}, as summarized in Table 1. The effective capacitances for the two CPEs, i.e., $C_{diel,eff}$ and $C_{dl,eff}$, were calculated using eqs 2 and 5, with R_{par}, the parallel summation of R_{CNT} and R_{ion}, utilized in eq 2. The chemi-impeditive sensor signal was expressed as the normalized change in circuit parameters, $\Delta X/X_0$ (%) = $(X - X_0)/X_0 \times 100$ (%), where X_0 represents the initial parameter value. The decrease in R_{CNT} is consistent with observations from chemiresistive measurements (Figure 5a). Tracking down R_{CNT} values over the course of PFAS injection enables us to obtain calibration curves for each PFAS species. Impedance responses were obtained upon adding various concentrations of PFAS solutions to the device (Figures S15−S18), yielding nonlinear response curves for R_{CNT}, as displayed in Figure 6b. Notably, their log−log plots exhibit linearity at sufficiently low concentration ranges (Figure 6c), suggesting that the interaction between PFAS and our f-SWCNT-based sensor may follow the Freundlich adsorption isotherm.[59,60] It is an empirical isotherm commonly employed in evaluating adsorption on heterogeneous surfaces. Its general form in the case of liquid solution environment is as follows

$$q_e = K_F C_e^{1/n} \tag{6}$$

$$\log q_e = \log K_F + \frac{1}{n}\log C_e \tag{7}$$

where q_e and C_e represent the amount of adsorbate per unit mass of adsorbent and the equilibrium concentration of the solution, respectively. K_F and n are empirical constants related to the adsorption capacity and macroscopic behavior of the adsorption system, where $0 < 1/n < 1$.[61] If the sensor response is proportional to the amount of adsorbate, the sensor signal will follow the Freundlich regime, which is plausible considering that the model has been frequently employed to analyze the adsorption of organic compounds on activated carbon or molecular sieves in aqueous systems.[62] As shown in Figures 6b,c, and S18, the sensor exhibits Freundlich responses ($R^2 > 0.99$) for PFOS, PFOA, GenX, and PFBS within the range of 10 nM−2 μM, 20 nM−10 μM, 1−20 μM, and 2−20 μM, respectively. We confirmed that R_{CNT} does not change upon adding DI water to the reservoir (see Figure S20). The sensor responses deviate from the Freundlich isotherm at higher concentration ranges, which is a common phenomenon because the Freundlich isotherm assumes unlimited surface coverage with no saturation effect.[63] The limit of detection (LOD) was calculated using the equation, LOD = $3.3s_Y/a$,[64] where the slope of response curve, a, was estimated near the lowest concentration points for each PFAS, resulting in ca. 8 ppb (PFOS), 20 ppb (PFOA), 0.49 ppm (GenX), and 0.75 ppm (PFBS), respectively. As presented in Figure S21, we also obtained calibration curves through DC-based chemiresistive measurement, which were very similar to the R_{CNT} responses obtained via EIS (Figure 6b,c). This observation is reasonable because R_{CNT} should be theoretically identical to such DC resistance under the same DC bias potential with no additional resistive components in series, if the dependence of CNT resistance on electrical potential is negligible. The shunt capacitors in TLM, Q_{dl}, open the circuit at sufficiently low frequencies (see Figure 3a).

Impedance analysis provides additional information about the system during the sensing process, such as R_{ion} and all the capacitive components, $C_{diel,eff}$ and $C_{dl,eff}$, all of which are technically impossible to measure with the conventional chemiresistive or chemicapacitive methods. The R_{ion} response for each PFAS shows similar trends, as can be seen in Figure 6d. At high [PFAS] (>10^{-5} M), R_{ion} slightly increases or decreases depending on the type of PFAS, and $\Delta R_{ion}/R_{ion,0}$ converges to ca. 6% as [PFAS] decreases. This trend is similar to the R_{ion} response observed when adding DI water (see Figure S20). In other words, each PFAS exhibits a distinct R_{ion} response depending on its unique ionic conductivity at high concentration, although this effect becomes indistinguishable at low concentration. As shown in Figure S22, $C_{diel,eff}$ did not change significantly throughout the entire concentration ranges for all PFAS, which accords with our expectations considering that the dielectric capacitance of the system is primarily related to the measurement environment, such as chip design and stray capacitance from surroundings. Conversely, each PFAS exhibits a distinct $C_{dl,eff}$ response as presented in Figure 6e. The responses with varying PFAS concentrations share a similar trend: the change ratio, $\Delta C_{dl,eff}/C_{dl,eff,0}$, decreases at relatively high concentration ranges and gradually increases until it reaches approximately −2.5% as [PFAS] decreases. The change in $C_{dl,eff}$ may be primarily caused by two factors: ionic strength of the reservoir and the specific interaction between PFAS and the f-SWCNT surface. The Gouy−Chapman capacitance is predicted to decrease with decreasing ion concentration. Therefore, adding an analyte solution with a lower ion concentration than the initial reservoir electrolyte would generally result in a lower $C_{dl,eff}$ due to the dilution of reservoir solution. It is expected that $\Delta C_{dl,eff}/C_{dl,eff,0}$ decreases from a certain initial value and becomes similar to the $\Delta C_{dl,eff}/C_{dl,eff,0}$ obtained from adding DI water to the reservoir (Figure S20) with decreasing [PFAS], which should be similar to the $C_{dl,eff}$ trend observed when adding HNO_3, as shown in Figure 6e. The specific binding of PFAS onto the f-SWCNT surface should also be considered to account for the observed $C_{dl,eff}$ response. We speculate that the strong binding of PFAS onto perfluoroalkyl ammonium groups on the f-SWCNT surface may decrease $C_{dl,eff}$ because the cationic surface moieties are already compensated by anionic PFAS in prior to applying any voltage to the system. This speculation is supported by most of the $\Delta C_{dl,eff}/C_{dl,eff,0}$ values for PFAS being below those from HNO_3 addition. Figure S23 indicates that the contribution from specific binding of NO_3^- onto the f-SWCNT surface is neglectable, given the R_{CNT} response. The f-SWCNT exhibits good repeatability and long-term stability when stored in the acidic baseline. The key chemi-impeditive responses, R_{CNT} and $C_{dl,eff}$, were retained over 6 weeks of aging (Figure S24). Although the overall CNT resistance gradually increased by approximately 4.5% over 50 repetitive chemi-impeditive measurements, the primary response parameters remained stable (Figure S25).

To gain a deeper understanding of the SWCNT-solution system, we first monitored changes in R_{ion} using EIS analysis while progressively increasing the volume of the 1 mM HCl(aq) reservoir electrolyte (Figure S26a), which showed negligible changes in the Nyquist plots. This implies that R_{ion} is

https://doi.org/10.1021/jacs.4c07986
J. Am. Chem. Soc. 2024, 146, 31486−31496

not primarily determined by the bulk ionic resistance of the reservoir electrolyte. As depicted in Figure S26b, we hypothesize that R_{ion} may be related to the ionic conduction of the electrolyte solution within the CNT network, composed of many percolating conductive pathways through CNTs. This model could be supported by additional EIS analyses of several p-SWCNT and f-SWCNT samples immersed in 1 mM HCl(aq) with varying R_{CNT} (Figure S27a). Figure S27b,c demonstrate that R_{ion} tends to rise as R_{CNT} increases. Considering that R_{CNT} would decrease with an increasing number of percolating pathways, a sample with lower R_{CNT} would have a larger CNT film volume and, hence a larger volume of electrolyte within the film for ion conduction, assuming a uniform CNT packing density in the film. In contrast, $C_{dl,eff}$ was observed to decrease as R_{CNT} increased, which is reasonable because $C_{dl,eff}$ will predominantly arise from the interface between the electrolyte and percolating CNTs electrically connected to both electrodes. Therefore, a sample with fewer percolating CNTs in the network, representing higher R_{CNT}, may have lower $C_{dl,eff}$. A more rigorous investigation of the CNT-electrolyte system will be crucial for the further development of chemi-impeditive sensors. Meanwhile, the f-SWCNT-based sensor showed similar sensor responses regardless of R_{CNT} level within the approximate range of 200 kΩ to 4 MΩ (Figure S28a). Due to the intrinsically low conductivity of f-SWCNT, likely resulting from covalent functionalization, it was technically very challenging to reach even lower R_{CNT} levels. As R_{CNT} exceeds several MΩs, the EIS spectrum begins to suffer from noise, especially in the low-frequency region (Figure S28b). Although this noise issue could be mitigated by using signal averaging, the extended measurement time could introduce another major problem: signal drift.

Finally, we leveraged the responses in R_{ion}, R_{CNT}, and $C_{dl,eff}$, to distinguish the PFAS analytes from each other via principal component analysis (PCA), as described in Figures 7a and S29. The combination of these three chemi-impeditive responses allows each PFAS to show a distinct trajectory in the 2D PCA plot as [PFAS] varies, which visualizes the discriminative detection although there is a cross point between PFOS and PFOA. The data points at high [PFAS] showing similar R_{CNT} (R_{DC}) responses due to the saturation effect can also be differentiated. As displayed in Figure 7b, the trajectories of the four PFAS converge as the concentration further decreases, which is plausible considering that the chemi-impeditive responses in R_{CNT}, R_{ion}, and $C_{dl,eff}$ become similar to those observed when adding DI water. Although the f-SWCNT is not in the highest group of PFAS sensors in terms of LOD for individual PFAS species (see Table S4), there is still few sensing methodology that allows for discriminative analyte detection at single-device level. Consequently, the unique affinity and degree of interaction between each PFAS and the f-SWCNT surface were reflected in the equivalent circuit parameters, by which several different analytes can be effectively differentiated via the chemi-impeditive method. We anticipate that novel surface engineering methods with an in-depth understanding of double layer capacitance and the analyte−surface interaction will endow even more marked differences in the equivalent circuit parameters.

CONCLUSIONS

We have reported a methodology implementing impedance spectroscopy for liquid analyte detection using SWCNTs.

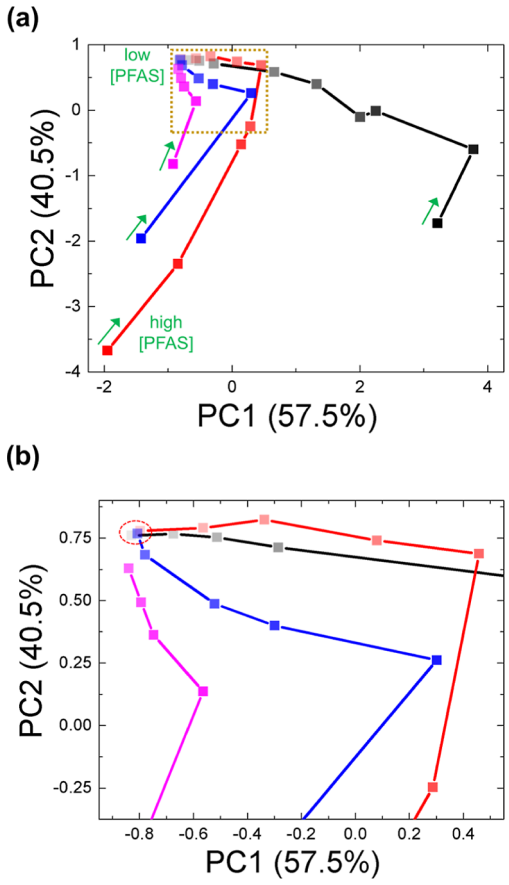

Figure 7. (a) PCA plots displaying detection of four individual PFAS using R_{CNT}, R_{ion}, and $C_{dl,eff}$ responses obtained from chemi-impeditive measurements in Figure 6: PFOS (black, 200 μM−10 nM), PFOA (red, 200 μM−20 nM), GenX (blue, 200−1 μM), and PFBS (magenta, 200−2 μM). All concentrations used are presented in Figures S15−S18. Each data point represents a set of chemi-impeditive data measured at each PFAS concentration. Green arrows indicate the direction of decreasing [PFAS]. For every decrease in [PFAS], a 10% increment of transparency is applied within the same color of data points. (b) Magnified view of the area marked with dark yellow dotted rectangle in (a). Red dotted circle indicates the data points for the lowest [PFOS], [PFOA], and [GenX].

Using a rigorous examination of the charge transport properties of a CNT layer in contact with an electrolyte solution, we successfully modeled the CNT-electrolyte system with an equivalent circuit involving TLM. This enables the analysis of unique impedance spectra from the CNT layer immersed in solution using EIS. Our approach of employing EIS for sensor signal measurement offers distinct advantages over conventional chemiresistive or chemicapacitive methods, as it provides comprehensive information on the equivalent circuit components including the capacitive contribution, solution resistance, as well as the CNT resistance. These multiple pieces of information, measurable through EIS, can be utilized complementarily to achieve the discriminative detection of a group of analytes at the single-device level. However, maintaining device quality is crucial, as factors such as the uniformity of the active material and the quality of electrical contact between the film and electrodes can significantly influence the impedance response. To demonstrate the effectiveness of our method, we developed a detection platform for PFAS in aqueous samples by

https://doi.org/10.1021/jacs.4c07986
J. Am. Chem. Soc. 2024, 146, 31486−31496

functionalizing the SWCNT surface with amine and perfluoroalkyl groups. The f-SWCNT exhibited p-type responses toward the four PFAS, i.e., PFOS, PFOA, GenX, and PFBS, which is consistent with their electron-deficient nature. Remarkably, these analytes were differentiated from each other and other ionic species through TLM-based equivalent circuit analysis using a single EIS measurement. The distinctive properties of each PFAS, including electronic properties, ionic conductivity, and binding affinity to the f-SWCNT, are reflected in the resistive and capacitive components of the measured impedance spectra such as R_{ion}, R_{CNT}, Q_{dl}, and n_{dl}.

The concept of chemi-impeditive sensing holds significant promise in the realm of chemical sensing. This methodology could potentially be extended to any conducting materials beyond SWCNTs, including conducting polymers. By implementing diverse surface modification chemistries, the sensing material can be tailored to exploit multidimensional impeditive information for discriminative detection of multiple analytes. We believe that leveraging the capacitive component will be pivotal in the development of such sensors, as it allows for novel information that can be synergized with conductivity data. Therefore, a detailed investigation of factors affecting the double layer capacitance of the material−electrolyte interface in the chemi-impeditive configuration will also be indispensable.

■ ASSOCIATED CONTENT

Supporting Information

The Supporting Information is available free of charge at https://pubs.acs.org/doi/10.1021/jacs.4c07986.

Materials and experimental methods; experimental details about the equivalent circuit study of the CNT-electrolyte system; detailed synthetic procedure for f-SWCNT, SEM images, and high-resolution XPS spectra; additional chemiresistive characterization data for p-SWCNT and f-SWCNT-based PFAS sensors; all the impedance spectra measured upon addition of PFOS, PFOA, GenX, and PFBS; additional chemi-impeditive data for f-SWCNT-based PFAS sensors (PDF)

■ AUTHOR INFORMATION

Corresponding Author

Timothy M. Swager − *Department of Chemistry, Massachusetts Institute of Technology, Cambridge, Massachusetts 02139, United States;* orcid.org/0000-0002-3577-0510; Email: tswager@mit.edu

Authors

Seok Hee Han − *Department of Chemistry, Massachusetts Institute of Technology, Cambridge, Massachusetts 02139, United States;* orcid.org/0000-0003-2518-278X

Thomas N. Pioch − *Department of Chemistry, Massachusetts Institute of Technology, Cambridge, Massachusetts 02139, United States;* orcid.org/0009-0000-7333-9732

Complete contact information is available at: https://pubs.acs.org/10.1021/jacs.4c07986

Author Contributions

The manuscript was written through contributions of all authors. All authors have given approval to the final version of the manuscript.

Notes

The authors declare no competing financial interest.

■ ACKNOWLEDGMENTS

This research was supported by Basic Science Research Program through the National Research Foundation of Korea (NRF) funded by the Ministry of Education (2021R1A6A3A03038924). We are grateful for support from Xylem Corporation and the MIT Jameel Water and Food Security Center and the National Science Foundation (DMR-2207299). This work was performed in part at Harvard University Center for Nanoscale Systems (CNS), a member of the National Nanotechnology Coordinated Infrastructure Network (NNCI), which is supported by the National Science Foundation under NSF award no. ECCS-2025158.

■ ABBREVIATIONS

TLM	transmission line model
EIS	electrochemical impedance spectroscopy
PFAS	perfluoroalkyl substances
MIEC	mixed ionic-electronic conductor
PFOS	perfluorooctanesulfonic acid
PFOA	perfluorooctanoic acid
GenX	hexafluoropropylene oxide dimer acid
PFBS	perfluorobutanesulfonic acid
p-SWCNT	pristine SWCNT
f-SWCNT	fluorinated SWCNT

■ REFERENCES

(1) Kauffman, D. R.; Star, A. Carbon Nanotube Gas and Vapor Sensors. *Angew. Chem., Int. Ed.* **2008**, *47*, 6550−6570.

(2) Schroeder, V.; Savagatrup, S.; He, M.; Lin, S.; Swager, T. M. Carbon Nanotube Chemical Sensors. *Chem. Rev.* **2019**, *119*, 599−663.

(3) Andre, R. S.; Ngo, Q. P.; Fugikawa-Santos, L.; Correa, D. S.; Swager, T. M. Wireless Tags with Hybrid Nanomaterials for Volatile Amine Detection. *ACS Sens.* **2021**, *6*, 2457−2464.

(4) Snow, E.; Perkins, F.; Houser, E.; Badescu, S.; Reinecke, T. Chemical Detection with a Single-Walled Carbon Nanotube Capacitor. *Science* **2005**, *307*, 1942−1945.

(5) Snow, E. S.; Perkins, F. K. Capacitance and Conductance of Single-Walled Carbon Nanotubes in the Presence of Chemical Vapors. *Nano Lett.* **2005**, *5*, 2414−2417.

(6) Robinson, J. A.; Snow, E.; Perkins, F. Improved Chemical Detection Using Single-Walled Carbon Nanotube Network Capacitors. *Sens. Actuators, A* **2007**, *135*, 309−314.

(7) Bezdek, M. J.; Luo, S.-X. L.; Liu, R. Y.; He, Q.; Swager, T. M. Trace Hydrogen Sulfide Sensing Inspired by Polyoxometalate-mediated Aerobic Oxidation. *ACS Cent. Sci.* **2021**, *7*, 1572−1580.

(8) Lu, Y.; Li, J.; Han, J.; Ng, H.-T.; Binder, C.; Partridge, C.; Meyyappan, M. Room Temperature Methane Detection Using Palladium Loaded Single-Walled Carbon Nanotube Sensors. *Chem. Phys. Lett.* **2004**, *391*, 344−348.

(9) Bezdek, M. J.; Luo, S.-X. L.; Ku, K. H.; Swager, T. M. A Chemiresistive Methane Sensor. *Proc. Natl. Acad. Sci. U.S.A.* **2021**, *118*, No. e2022515118.

(10) Luo, S.-X. L.; Lin, C.-J.; Ku, K. H.; Yoshinaga, K.; Swager, T. M. Pentiptycene Polymer/Single-Walled Carbon Nanotube Complexes: Applications in Benzene, Toluene, and o-Xylene Detection. *ACS Nano* **2020**, *14*, 7297−7307.

(11) Fennell, J. F.; Hamaguchi, H.; Yoon, B.; Swager, T. M. Chemiresistor Devices for Chemical Warfare Agent Detection Based on Polymer Wrapped Single-Walled Carbon Nanotubes. *Sensors* **2017**, *17*, 982.

(12) Horrillo, M.; Martí, J.; Matatagui, D.; Santos, J.; Sayago, I.; Gutiérrez, J.; Martin-Fernandez, I.; Ivanov, P.; Gràcia, I.; Cané, C.

Single-Walled Carbon Nanotube Microsensors for Nerve Agent Simulant Detection. *Sens. Actuators, B* **2011**, *157*, 253−259.
(13) Zhu, R.; Azzarelli, J. M.; Swager, T. M. Wireless Hazard Badges to Detect Nerve-Agent Simulants. *Angew. Chem., Int. Ed.* **2016**, *55*, 9662−9666.
(14) Choi, S.-J.; Yoon, B.; Lin, S.; Swager, T. M. Functional Single-Walled Carbon Nanotubes for Anion Sensing. *ACS Appl. Mater. Interfaces* **2020**, *12*, 28375−28382.
(15) Choi, S. J.; Yoon, B.; Ray, J. D.; Netchaev, A.; Moores, L. C.; Swager, T. M. Chemiresistors for the Real-Time Wireless Detection of Anions. *Adv. Funct. Mater.* **2020**, *30*, 1907087.
(16) Jing, H. J.; Jiang, Y. D.; Du, X. S. The Effect of Density and Surface Area on Carbon Nanotube Capacitive Sensors for Dimethyl Methylphosphonate Detection. *Key Eng. Mater.* **2012**, *531*−*532*, 519−522.
(17) Song, S. G.; Ha, S.; Cho, H. J.; Lee, M.; Jung, D.; Han, J.-H.; Song, C. Single-Walled Carbon-Nanotube-Based Chemocapacitive Sensors with Molecular Receptors for Selective Detection of Chemical Warfare Agents. *ACS Appl. Nano Mater.* **2019**, *2*, 109−117.
(18) Kim, S.; Lee, K.-H.; Lee, J.-Y.; Kim, K.-K.; Choa, Y.-H.; Lim, J.-H. Single-Walled Carbon Nanotube-Based Chemi-Capacitive Sensor for Hexane and Ammonia. *Electron. Mater. Lett.* **2019**, *15*, 712−719.
(19) Lasia, A. *Electrochemical Impedance Spectroscopy and Its Applications*; Springer, 2014.
(20) Varghese, O.; Kichambre, P.; Gong, D.; Ong, K.; Dickey, E.; Grimes, C. Gas Sensing Characteristics of Multi-Wall Carbon Nanotubes. *Sens. Actuators, B* **2001**, *81*, 32−41.
(21) Brahim, S.; Colbern, S.; Gump, R.; Grigorian, L. Tailoring Gas Sensing Properties of Carbon Nanotubes. *J. Appl. Phys.* **2008**, *104*, 024502.
(22) Brahim, S.; Colbern, S.; Gump, R.; Moser, A.; Grigorian, L. Carbon Nanotube-Based Ethanol Sensors. *Nanotechnology* **2009**, *20*, 235502.
(23) Lenka, S. P.; Kah, M.; Padhye, L. P. A Review of the Occurrence, Transformation, and Removal of Poly- and Perfluoroalkyl Substances (PFAS) in Wastewater Treatment Plants. *Water Res.* **2021**, *199*, 117187.
(24) Whitehead, H. D.; Venier, M.; Wu, Y.; Eastman, E.; Urbanik, S.; Diamond, M. L.; Shalin, A.; Schwartz-Narbonne, H.; Bruton, T. A.; Blum, A.; et al. Fluorinated Compounds in North American Cosmetics. *Environ. Sci. Technol. Lett.* **2021**, *8*, 538−544.
(25) Trier, X.; Granby, K.; Christensen, J. H. Polyfluorinated Surfactants (PFS) in Paper and Board Coatings for Food Packaging. *Environ. Sci. Pollut. Res.* **2011**, *18*, 1108−1120.
(26) Dauchy, X.; Boiteux, V.; Bach, C.; Rosin, C.; Munoz, J.-F. Per- and Polyfluoroalkyl Substances in Firefighting Foam Concentrates and Water Samples Collected near Sites Impacted by the Use of These Foams. *Chemosphere* **2017**, *183*, 53−61.
(27) Glüge, J.; Scheringer, M.; Cousins, I. T.; DeWitt, J. C.; Goldenman, G.; Herzke, D.; Lohmann, R.; Ng, C. A.; Trier, X.; Wang, Z. An Overview of the Uses of Per- and Polyfluoroalkyl Substances (PFAS). *Environ. Sci.: Processes Impacts* **2020**, *22*, 2345−2373.
(28) Concellón, A.; Swager, T. M. Detection of Per-and Polyfluoroalkyl Substances (PFAS) by Interrupted Energy Transfer. *Angew. Chem., Int. Ed.* **2023**, *62*, No. e202309928.
(29) Panieri, E.; Baralic, K.; Djukic-Cosic, D.; Buha Djordjevic, A.; Saso, L. PFAS Molecules: A Major Concern for the Human Health and the Environment. *Toxics* **2022**, *10*, 44.
(30) Pelch, K. E.; Reade, A.; Wolffe, T. A.; Kwiatkowski, C. F. PFAS Health Effects Database: Protocol for a Systematic Evidence Map. *Environ. Int.* **2019**, *130*, 104851.
(31) Concellón, A.; Castro-Esteban, J.; Swager, T. M. Ultratrace PFAS Detection Using Amplifying Fluorescent Polymers. *J. Am. Chem. Soc.* **2023**, *145*, 11420−11430.
(32) Harrison, E. E.; Waters, M. L. Detection and Differentiation of Per- and Polyfluoroalkyl Substances (PFAS) in Water Using a Fluorescent Imprint-and-Report Sensor Array. *Chem. Sci.* **2023**, *14*, 928−936.
(33) Chen, B.; Yang, Z.; Qu, X.; Zheng, S.; Yin, D.; Fu, H. Screening and Discrimination of Perfluoroalkyl Substances in Aqueous Solution Using a Luminescent Metal−Organic Framework Sensor Array. *ACS Appl. Mater. Interfaces* **2021**, *13*, 47706−47716.
(34) Guryanov, I.; Toma, F. M.; Montellano López, A.; Carraro, M.; Da Ros, T.; Angelini, G.; D'Aurizio, E.; Fontana, A.; Maggini, M.; Prato, M. Microwave-Assisted Functionalization of Carbon Nanostructures in Ionic Liquids. *Chemistry* **2009**, *15*, 12837−12845.
(35) Weizmann, Y.; Chenoweth, D. M.; Swager, T. M. DNA−CNT Nanowire Networks for DNA Detection. *J. Am. Chem. Soc.* **2011**, *133*, 3238−3241.
(36) Liu, S. F.; Lin, S.; Swager, T. M. An Organocobalt−Carbon Nanotube Chemiresistive Carbon Monoxide Detector. *ACS Sens.* **2016**, *1*, 354−357.
(37) Delalande, M.; Clavaguera, S.; Toure, M.; Carella, A.; Lenfant, S.; Deresmes, D.; Vuillaume, D.; Simonato, J.-P. Chemical Functionalization of Electrodes for Detection of Gaseous Nerve Agents with Carbon Nanotube Field-Effect Transistors. *Chem. Commun.* **2011**, *47*, 6048−6050.
(38) He, M.; Croy, R. G.; Essigmann, J. M.; Swager, T. M. Chemiresistive Carbon Nanotube Sensors for N-Nitrosodialkylamines. *ACS Sens.* **2019**, *4*, 2819−2824.
(39) Fong, D.; Luo, S.-X. L.; Andre, R. S.; Swager, T. M. Trace Ethylene Sensing via Wacker Oxidation. *ACS Cent. Sci.* **2020**, *6*, 507−512.
(40) Lasia, A. The Origin of the Constant Phase Element. *J. Phys. Chem. Lett.* **2022**, *13*, 580−589.
(41) Chang, B.-Y. Conversion of a Constant Phase Element to an Equivalent Capacitor. *J. Electrochem. Sci. Technol.* **2020**, *11*, 318−321.
(42) Hebb, M. H. Electrical Conductivity of Silver Sulfide. *J. Chem. Phys.* **1952**, *20*, 185−190.
(43) Yokota, I. On the Theory of Mixed Conduction with Special Reference to Conduction in Silver Sulfide Group Semiconductors. *J. Phys. Soc. Jpn.* **1961**, *16*, 2213−2223.
(44) Jamnik, J.; Maier, J. Treatment of the Impedance of Mixed Conductors Equivalent Circuit Model and Explicit Approximate Solutions. *J. Electrochem. Soc.* **1999**, *146*, 4183−4188.
(45) Jamnik, J.; Maier, J.; Pejovnik, S. A Powerful Electrical Network Model for the Impedance of Mixed Conductors. *Electrochim. Acta* **1999**, *44*, 4139−4145.
(46) Jamnik, J.; Maier, J. Generalised Equivalent Circuits for Mass and Charge Transport: Chemical Capacitance and Its Implications. *Phys. Chem. Chem. Phys.* **2001**, *3*, 1668−1678.
(47) Ahn, P.-A.; Shin, E.-C.; Kim, G.-R.; Lee, J.-S. Application of Generalized Transmission Line Models to Mixed Ionic-Electronic Transport Phenomena. *J. Korean Ceram. Soc.* **2011**, *48*, 549−558.
(48) Lai, W.; Haile, S. M. Impedance Spectroscopy as a Tool for Chemical and Electrochemical Analysis of Mixed Conductors: A Case Study of Ceria. *J. Am. Ceram. Soc.* **2005**, *88*, 2979−2997.
(49) Shin, E.-C.; Seo, H.-H.; Kim, J.-H.; Ahn, P.-A.; Park, S. M.; Lim, Y. W.; Kim, S. J.; Kim, C. H.; Kim, D. J.; Hong, C. K.; et al. A New Diagnostic Tool for the Percolating Carbon Network in the Polymer Matrix. *Polymer* **2013**, *54*, 999−1003.
(50) Cao, D.; Pang, P.; Liu, H.; He, J.; Lindsay, S. Electronic Sensitivity of a Single-Walled Carbon Nanotube to Internal Electrolyte Composition. *Nanotechnology* **2012**, *23*, 085203.
(51) Bard, A. J.; Faulkner, L. R. *Electrochemical Methods: Fundamentals and Applications*; John Wiley, 2001.
(52) Dresselhaus, M. S.; Dresselhaus, G.; Saito, R.; Jorio, A. Raman Spectroscopy of Carbon Nanotubes. *Phys. Rep.* **2005**, *409*, 47−99.
(53) Kundu, S.; Xia, W.; Busser, W.; Becker, M.; Schmidt, D. A.; Havenith, M.; Muhler, M. The Formation of Nitrogen-Containing Functional Groups on Carbon Nanotube Surfaces: A Quantitative XPS and TPD Study. *Phys. Chem. Chem. Phys.* **2010**, *12*, 4351−4359.
(54) Zhou, X.; Yang, H.; Wang, F. [BMIM] BF_4 Ionic Liquids as Effective Inhibitor for Carbon Steel in Alkaline Chloride Solution. *Electrochim. Acta* **2011**, *56*, 4268−4275.
(55) Wagner, C. D. NIST X-ray Photoelectron Spectroscopy Database. *NIST Standard Reference Database 20*, 2000.

https://doi.org/10.1021/jacs.4c07986
J. Am. Chem. Soc. 2024, 146, 31486−31496

(56) Huque, F. T.; Jones, K.; Saunders, R. A.; Platts, J. A. Statistical and Theoretical Studies of Fluorophilicity. *J. Fluorine Chem.* **2002**, *115*, 119−128.
(57) Lei, X.; Lian, Q.; Zhang, X.; Karsili, T. K.; Holmes, W.; Chen, Y.; Zappi, M. E.; Gang, D. D. A Review of PFAS Adsorption from Aqueous Solutions: Current Approaches, Engineering Applications, Challenges, and Opportunities. *Environ. Pollut.* **2023**, *321*, 121138.
(58) Medina, P. B.; Cotty, S.; Kim, K.; Elbert, J.; Su, X. Emerging Investigator Series: Electrochemically-mediated Remediation of GenX Using Redox-copolymers. *Environ. Sci.: Water Res. Technol.* **2021**, *7*, 2231−2240.
(59) Azizian, S.; Eris, S. Adsorption Isotherms and Kinetics. *Interface Science and Technology*; Elsevier, 2021; Vol. *33*, pp 445−509.
(60) Kalam, S.; Abu-Khamsin, S. A.; Kamal, M. S.; Patil, S. Surfactant Adsorption Isotherms: A Review. *ACS Omega* **2021**, *6*, 32342−32348.
(61) Yang, C.-h. Statistical Mechanical Study on the Freundlich Isotherm Equation. *J. Colloid Interface Sci.* **1998**, *208*, 379−387.
(62) Ahmaruzzaman, M. Adsorption of Phenolic Compounds on Low-cost Adsorbents: A Review. *Adv. Colloid Interface Sci.* **2008**, *143*, 48−67.
(63) Umpleby, R. J., II; Baxter, S. C.; Bode, M.; Berch, J. K., Jr.; Shah, R. N.; Shimizu, K. D. Application of the Freundlich Adsorption Isotherm in the Characterization of Molecularly Imprinted Polymers. *Anal. Chim. Acta* **2001**, *435*, 35−42.
(64) Hayashi, Y.; Matsuda, R.; Ito, K.; Nishimura, W.; Imai, K.; Maeda, M. Detection Limit Estimated from Slope of Calibration Curve: An Application to Competitive ELISA. *Anal. Sci.* **2005**, *21*, 167−169.

https://doi.org/10.1021/jacs.4c07986
J. Am. Chem. Soc. 2024, 146, 31486−31496